



Molecular basis for curvature formation in SepF polymerization

Wenjing Liu^{a,b,1}, Chang Zhang^{a,1}, Huawei Zhang^{c,d,1} , Shaojie Ma^a, Jing Deng^a, Daping Wang^{d,e} , Ziwei Chang^{a,2}, and Jun Yang^{a,f,2}

Edited by Robert Tycko, National Institute of Diabetes and Digestive and Kidney Diseases, Bethesda, MD; received October 8, 2023; accepted November 20, 2023

The self-assembly of proteins into curved structures plays an important role in many cellular processes. One good example of this phenomenon is observed in the septum-forming protein (SepF), which forms polymerized structures with uniform curvatures. SepF is essential for regulating the thickness of the septum during bacteria cell division. In *Bacillus subtilis*, SepF polymerization involves two distinct interfaces, the β - β and α - α interfaces, which define the assembly unit and contact interfaces, respectively. However, the mechanism of curvature formation in this step is not yet fully understood. In this study, we employed solid-state NMR (SSNMR) to compare the structures of cyclic wild-type SepF assemblies with linear assemblies resulting from a mutation of G137 on the β - β interface. Our results demonstrate that while the sequence differences arise from the internal assembly unit, the dramatic changes in the shape of the assemblies depend on the α - α interface between the units. We further provide atomic-level insights into how the angular variation of the α helix on the α - α interface affects the curvature of the assemblies, using a combination of SSNMR, cryo-electron microscopy, and simulation methods. Our findings shed light on the shape control of protein assemblies and emphasize the importance of interhelical contacts in retaining curvature.

self-assembly | solid-state NMR | curvature | cell division | interface

In organism, many proteins perform their biological functions by self-assembling into various topological structures. Examples include the regularly arranged fibrils of cuticular protein and chitin and the helical assemblies of tobacco mosaic virus (TMV) (1, 2). Protein self-assemblies with curved shapes represent a class of biological structures that are closely related to catalysis, signaling, membrane bending, DNA binding, cytoskeletal functions, and more (3, 4). For instance, BAR (Bin/amphiphysin/Rvs) domain proteins can confer membrane curvature in a range of diameters and participate in numerous membrane-curving processes (5, 6). Many ring-shaped proteins are involved in the processivity of DNA polymerases, unwinding of DNA, and DNA recombination (7, 8). In most cases, protein can spontaneously form assembled structures; hence, controlling the curvature of the assemblies is particularly crucial for understanding their function. However, determining the structure of curved self-assemblies is often challenging, and a comprehensive understanding of curvature formation requires further investigation.

The control of curvature in self-assemblies is influenced by various factors, including the flexibility and conformation of the assembly units, as well as the driving forces between them. For instance, bacterial Vipp1 and PspA can form rings with varying curvatures, ranging from semiopen to fully open conformations, whereas they form rigid filaments by arranging the closed conformation (9–12). In the field of supramolecular and macromolecular chemistry, several types of driving forces have been identified for controlling the morphology of protein self-assembly in the construction of protein superstructures (13–15). However, the mechanism underlying the formation of stable curvatures in many proteins remains poorly understood, particularly in terms of the atomic details of curvature changes.

SepF is a cell division protein that plays a crucial role in anchoring FtsZ to the cytoplasmic membrane. It is found in a wide range of bacterial species, including gram-positive bacteria, cyanobacteria, and archaea. In many bacterial species, the function of SepF is associated with membrane remodeling, which requires protein polymerization (16–18). The curvature of SepF polymers has been demonstrated to have biological significance in controlling septal thickness, as highlighted by Wenzel et al. in their study on *Bacillus subtilis* (19). Importantly, the formation of SepF rings can influence the alignment of FtsZ, thereby affecting cell growth. Previous investigations have indicated that the replacement of wild-type (WT) SepF with the G137N variant, which breaks the ring, leads to an inability of the *B. subtilis* strain to sustain bacteria growth (20). However, the precise mechanism of SepF polymerization and curvature formation remains unclear, as the polymer structure of SepF has not yet been reported.

Significance

The formation of curved protein assemblies is crucial for various biological functions. Septum-forming protein (SepF) assembly, in particular, plays a crucial role in regulating septum thickness during bacterial cell division. Previous studies have shown that mutations of Gly137 disrupt the ring formation of *Bacillus subtilis* SepF, negatively impacting bacterial growth. However, the underlying mechanisms are not fully understood. To address this, we used solid-state NMR to study changes in SepF assembly shape. Our findings revealed that morphological changes depend on the assembly unit interface. Additionally, our atomic model elucidated how angular variations in α -helical contacts affect assembly curvature. These insights emphasize the importance of interhelical contacts in maintaining curvature and have implications for designing supramolecular self-assemblies.

Author contributions: Z.C. and J.Y. designed research; W.L., C.Z., H.Z., S.M., J.D., and Z.C. performed research; W.L., C.Z., H.Z., S.M., and Z.C. analyzed data; and W.L., C.Z., H.Z., D.W., Z.C., and J.Y. wrote the paper.

The authors declare no competing interest.

This article is a PNAS Direct Submission.

Copyright © 2024 the Author(s). Published by PNAS. This article is distributed under Creative Commons Attribution-NonCommercial-NoDerivatives License 4.0 (CC BY-NC-ND).

¹W.L., C.Z., and H.Z. contributed equally to this work.

²To whom correspondence may be addressed. Email: zwchang@wipm.ac.cn or yangjun@wipm.ac.cn.

This article contains supporting information online at <https://www.pnas.org/lookup/suppl/doi:10.1073/pnas.2316922121/-DCSupplemental>.

Published February 21, 2024.

In *B. subtilis*, the assembly of SepF involves two interfaces: the α - α interface and the β - β interface. This raises the intriguing question of which interface is responsible for the curved structure. Previous studies have proposed that the dimer, formed by the β -sheets of two monomers, serves as the functional unit of SepF polymers, as revealed by the crystal structure of N-terminal truncated SepF (17). However, the specific contacts and interactions occurring at the α - α interface have not been well established or fully characterized.

Solid-state NMR (SSNMR) offers unique advantages for studying molecular interactions in supramolecular self-assemblies, primarily due to the high sensitivity of NMR chemical shifts to local environments (21–24). In this study, our objective was to investigate the potential transition mechanism between different curvature assemblies of *B. subtilis* SepF. Specifically, we sought to identify the key amino acid site that drives continuous curvature changes and gives rise to different polymer shapes. To achieve this, we employed SSNMR as a tool to probe curvature-induced conformational changes between linear and cyclic SepF assemblies. Additionally, we complemented our experimental findings with cryo-electron microscopy (cryo-EM) and simulation methods to analyze the molecular basis underlying curvature formation. By integrating these techniques, we aimed to provide a comprehensive understanding of the mechanisms governing curvature transitions in SepF assemblies.

Results

Mutations on G137 of SepF Induced Different Shapes of Protein Assembly. In *B. subtilis* SepF polymerization, the β - β interface was thought to define the functional unit, and the α - α interface was believed to be involved in ring formation (17, 20). The disruption of the α - α interface can lead to depolymerization of the protein. Meanwhile, a G137N mutation on the β - β interface affected the shape of SepF assembly, leading to the formation of filamentous structures. To investigate whether this change occurs regularly and how it works, we extended research on the impacts of G137 residue. The homogeneous analysis demonstrated that G137 was quite conserved across gram-positive bacteria (Fig. 1A). Several variants were made by substitution of G137 with different types of amino acids, depending on the properties of the side chains. Representative mutants were G137A and G137I with aliphatic R groups, G137F and G137Y with aromatic R groups, G137N with a polar but uncharged R group, G137R and G137K with positively charged R groups, and G137D with a negatively charged R group (Fig. 1A). Afterward, size-exclusion chromatography (SEC) and electron microscopy (EM) analysis were performed to characterize the polymerization state of SepF. As a result, the same shape as WT SepF was formed in mutations of G137F and G137I, which can be demonstrated by the nearly identical elution volume in SEC and ring structures with a similar size in EM (Fig. 1B and C). On the other hand, the replacement of G137 with Asn, Lys, and Arg generated linear fibrillar structures. Specifically, the elution profile of these mutants showed undulating peaks, yet all fractions were found to be composed of fibrils (SI Appendix, Fig. S1 A and B). Another type of substitutions (to Ala, Asp, and Tyr) leads to oligomeric structures, where the elution profile of each mutation showed a single peak at 13 to 14 mL, with a corresponding molecular weight of approximately 50 to 100 kDa (4 to 8 monomers).

The CD spectra of WT SepF and its variants exhibited consistent shapes of spectral peaks (SI Appendix, Fig. S1), indicating similar secondary structures between the variants and the WT. However, there were slight differences in the CD values among

the samples. Notably, the G137R mutant showed a specific peak around 200 nm, which was not observed in the other samples. To further investigate the secondary structure, we assigned the chemical shifts of WT, G137N, G137F, and G137R and used TALOS+ for secondary structure prediction (SI Appendix, Figs. S2 and S3). The SSNMR analysis revealed nearly identical secondary structures between the WT and variant proteins. CD estimation of β -sheet-containing proteins can be challenging due to their diverse morphological and spectral characteristics (25). NMR chemical shifts provide a reliable method for estimating the secondary structural content of α -helices and β -strands in protein assemblies.

The above results suggest that the significant changes observed in the protein assembly shape were not solely due to the breaking or formation of chemical bonds at the β - β interface, indicating the presence of other contributing factors.

Conformation Changes from Cyclic to Linear Assembly Mainly Located at the α 2 Helix. To illustrate the structural mechanism underlying the shape changes of SepF assembly, we detected the chemical shift perturbations (CSPs) between cyclic and linear SepF assemblies. Although the mutants showed differences in the chromatograph, they exhibited good resolution in SSNMR spectra, indicating highly homogenous conformations. As a representative linear and cyclic assembly, we selected G137N and G137F, respectively. The SSNMR spectra were compared to that of WT-SepF. In brief, the perturbations (labeled as group I) between G137N and WT-SepF spectra may be attributed to two types of factors: the mutation and the shape change. While for another pair of comparison between G137F and WT-SepF, the perturbations (labeled as group II) are derived from a single factor of mutation. Thus, shape change-induced structural perturbations belong to the residues in group I by excluding the group II perturbations.

All three samples displayed excellent resolution and dispersities, thus allowing for the distinction of atomic-level differences. A set of 2D and 3D experiments including NCA, DARR, NCACX, NCOCX, and CONCA were acquired on the G137N and G137F samples (SI Appendix, Table S1), and the assignments were accomplished referring to that of WT SepF (26), as shown in SI Appendix, Tables S2 and S3. The sequence backbone walks and representative sequential assignments were shown in SI Appendix, Figs. S4 and S5. A comparison of the predicted secondary structure of WT, G137F, and G137N showed that they were almost identical, except that the lengths of the β strands were slightly different (SI Appendix, Figs. S6 and S7). Superpositions of 2D ^{15}N - ^{13}C correlation spectra showed overall similar shapes, with most peaks overlapped but several observable CSPs between WT and two variants (Fig. 2A). Correlation of side-chain ^{13}C signals to the respective backbone nitrogen signals by 2D NcaCX spectra showed more CSPs (SI Appendix, Fig. S8). Meanwhile, the good quality of resolution and signal intensity of the 3D SSNMR spectrum enabled us to identify comprehensive changes (SI Appendix, Fig. S9).

The weighted chemical shift changes ($\Delta\delta$) between G137N and WT-SepF were characterized and presented in SI Appendix, Fig. S10 and Table S4. Using the common method of severing the average value of chemical shift changes as significant changes, all residues with $\Delta\delta \geq 0.4$ ppm were counted. A total of thirty-four residues in G137N were identified and classified as group I. They have a wide distribution along the protein sequence, mainly in V64-R70 (β 1), R85-L92 (β 2), D98-I114 (α 2), and S123-S136 (β 4 and β 5) (Fig. 2B). Next, we identified the group II residues representing mutation-affected CSPs by comparing the spectra of G137F and WT-SepF. Twenty-one residues were found to have $\Delta\delta \geq 0.4$ ppm, mainly located at β 1, β 2, β 4, and β 5 (SI Appendix, Table S5).

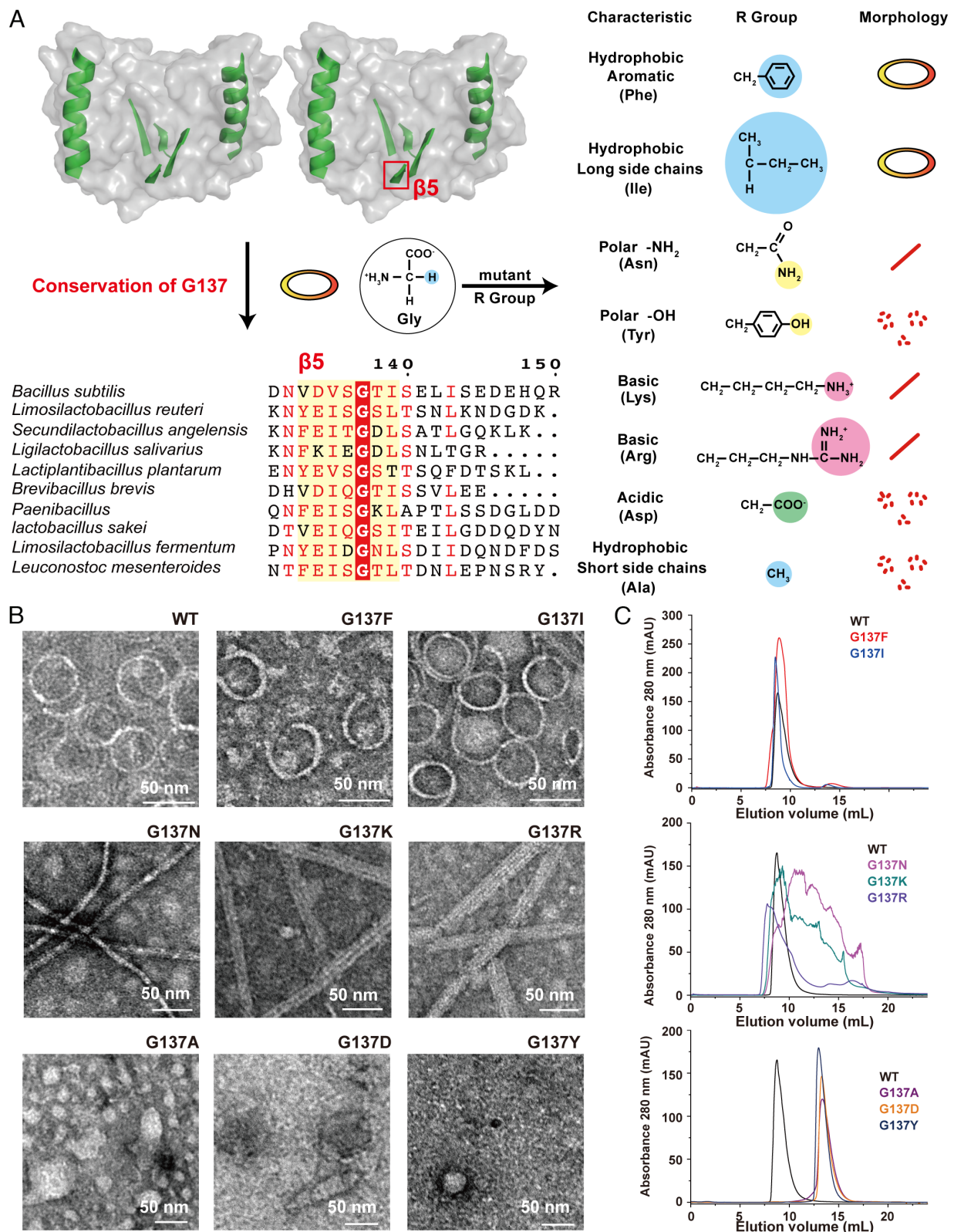


Fig. 1. Morphological changes of SepF self-assemblies upon point mutations on the conserved residue G137 in β 5. (A) Schematic depiction shows the location of G137 and mutation strategies. Two distinct types of interfaces existed in SepF assembly are colored in green, with G137 colored in red locating at β 5. Sequence alignment of β 5 (shaded residues) among several gram-positive bacteria shows high conservation of Gly137. The morphologies of SepF after mutation are determined and indicated as ring (cyclic), stick (linear), and splashes (oligomers). (B) Negative-stain TEM images of ring, fibril, and oligomer in assembly buffer. (Scale bars, 50 nm.) (C) Elution profile of gel-filtration chromatographic of the WT and different variants of SepF.

The vast majority of the residues in group II were included in group I. After excluding these residues shared in common, the remaining residues in group I were decisive for curvature change from cyclic

to linear assemblies. They were: V65, L66, Y72, H81, V88, V90, D98, Q99, K101, V104, D105, G109, Y112, A113, G116, and D134 (Fig. 2 B and C). These residues have a main distribution at

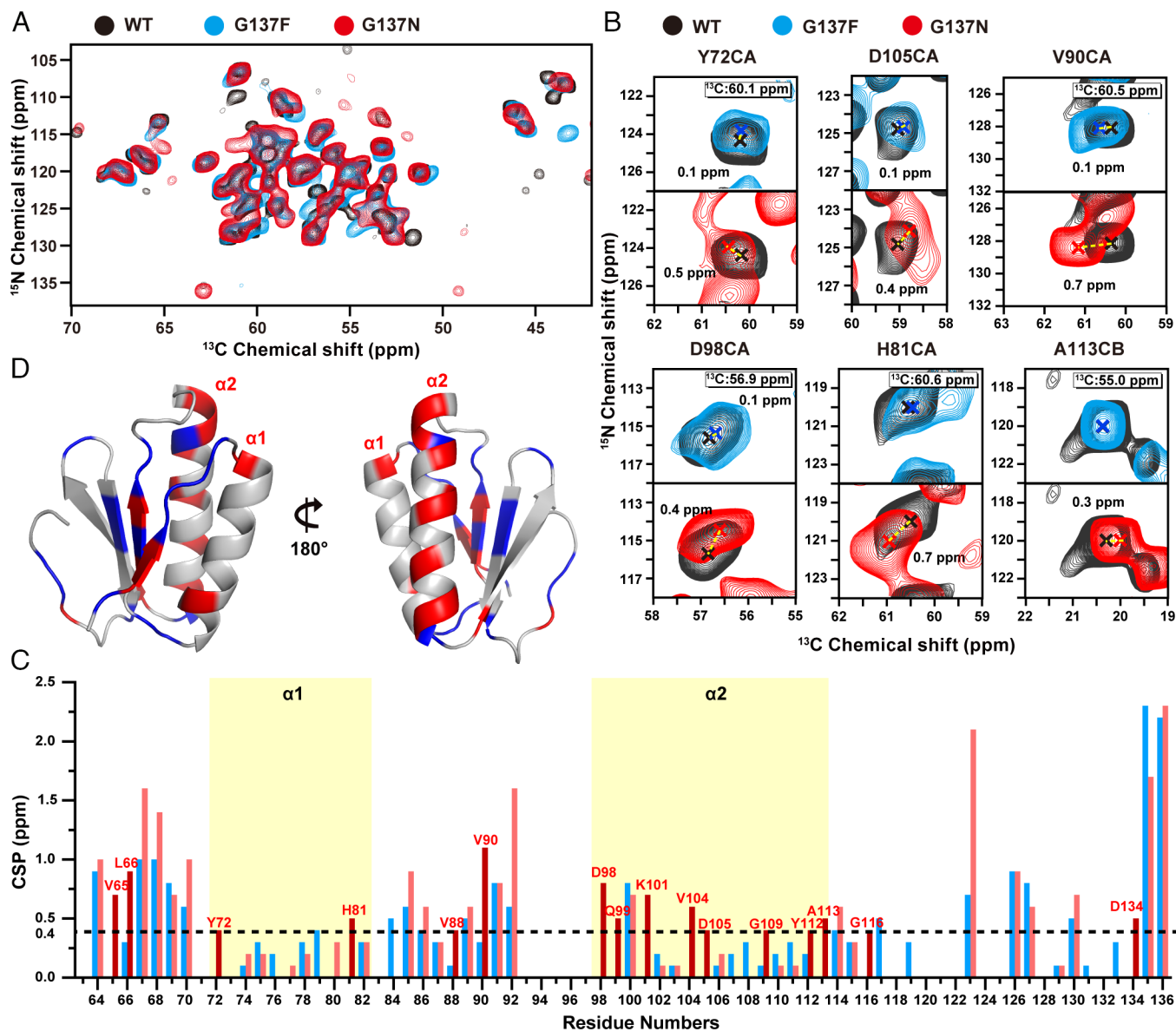


Fig. 2. SSNMR spectra showing the specific changes between cyclic and linear SepF assembly. (A) Superposition of 2D ^{15}N - $^{13}\text{C}_{\alpha}$ (NCA) spectra of the WT (black), G137F (cyan), and G137N SepF (red). (B) Detailed views of SSNMR spectra show obvious CSPs between G137N, G137F, and WT SepF. All the views are exacted from the 2D NcaCX spectra and 3D NCACX spectra. (C) The histogram shows the values of $\Delta\delta$ (WT-G137F) (cyan) and $\Delta\delta$ (WT-G137N) (red). Dashed lines indicate the standard of the $\Delta\delta$ value corresponding to the D_d value of 0.4. The residues with specific CSPs in G137N are labeled by residue names and numbers while their bars are emphasized by scarlet. (D) Critical residue sites are marked on the monomeric structure calculated by CS-Rosetta (26) in two views. Perturbed residues in both G137F and G137N are labeled in blue, while perturbed residues only in G137N are labeled by red color.

the α_2 helix. Mapping of these changes in the structural model of SepF was shown in Fig. 2D. Interestingly, most of the changes occurs at the outside surface of α_2 . It is worth mentioning that there appeared to be less glycine in the mutant spectra, which was identified to be Gly122 missing. In fact, the residue belongs to a loop region of I121-I125 that is relatively dynamic and exhibits a low S/N ratio. One possible explanation is that the mutations could affect the dynamics of the loop region, causing it to become more flexible.

To further investigate whether the behavior in G137N is an isolated incident or regular pattern, we characterized the CSPs between WT-SepF and other variants of fibril, G137K, and G137R-SepF (*SI Appendix*, Tables S6–S9). As expected, all fibrillar samples showed almost identical spectra, and specific chemical changes in the helix were observed in G137K and G137R variants. As shown in *SI Appendix*, Fig. S11, eleven residues were identified

to have significant changes in CSPs in each variant, relating to morphological changes. The chemical shifts of those residues in WT (black) and G137F (cyan) were almost the same, but perturbed similarly in the three linear fibril samples G137N (red), G137K (yellow), and G137R (green).

Taken together, the above results strongly suggest that although the mutation occurs inside the structural unit of SepF, the shape changes result from the α - α interface changes upon dimer polymerization.

Integrated Cryo-EM and SSNMR Structure Calculation of G137N SepF Fibril. To further characterize how these changes affect the assembling of the dimers, we then proceeded to solve the self-assembled structure of ring-like and fibrillar SepF. Although SSNMR can deliver abundant structural information, allowing protein structure determination at the atomic level, the process

is particularly challenging. Instead, we considered cryo-EM in our study, which is presently the most powerful tool for structure determination of protein macromolecules.

The two samples of WT and G137N SepF were prepared as described above for SSNMR samples and applied to an electron microscopy grid in solution. The utilization of cryo-EM for studying the rings of WT SepF encountered significant difficulties due to the nonuniform diameter and irregular circular shape of the rings. On the other hand, the fibrillar G137N SepF yielded homogeneous morphology, but with diverse forms as shown in the cryo-EM micrograph. The filament can be in a thin form or in a twisted belt form when thin form aligned together (Fig. 3A). Due to the challenge in data processing, only the thin form of filament was considered in the following data processing. The thin-form filament was picked, extracted, and subject to 2D classification (SI Appendix, Fig. S12). High-quality 2D classes showed that SepF

filament was possibly formed by the stacking of homodimers, with a 180° rotation between adjacent promoters (Fig. 3B). An initial model was generated, optimized, and refined to get the final map with overall resolution of 7.32 Å (Fig. 3C and D and SI Appendix, Table S10). The resulting map clearly exhibited the linear arrangement of SepF monomers. However, at this relatively low resolution, it is still challenging to obtain atomic information.

The strategy of combining data from SSNMR and cryo-EM has been proved to be useful for the determination of atomic-resolution protein structures (27–29). In these cases, the structures or NMR chemical shifts were used for rigid or flexible fitting to EM densities. Here, we performed MDFF simulation to fit the dimeric CS-ROSETTA model of G137N SepF into the cryo-EM map. The CS-ROSETTA strategy allows de novo protein structure generation with high reliability and accuracy, using chemical shifts as input parameters (21). The monomeric structure of WT SepF has

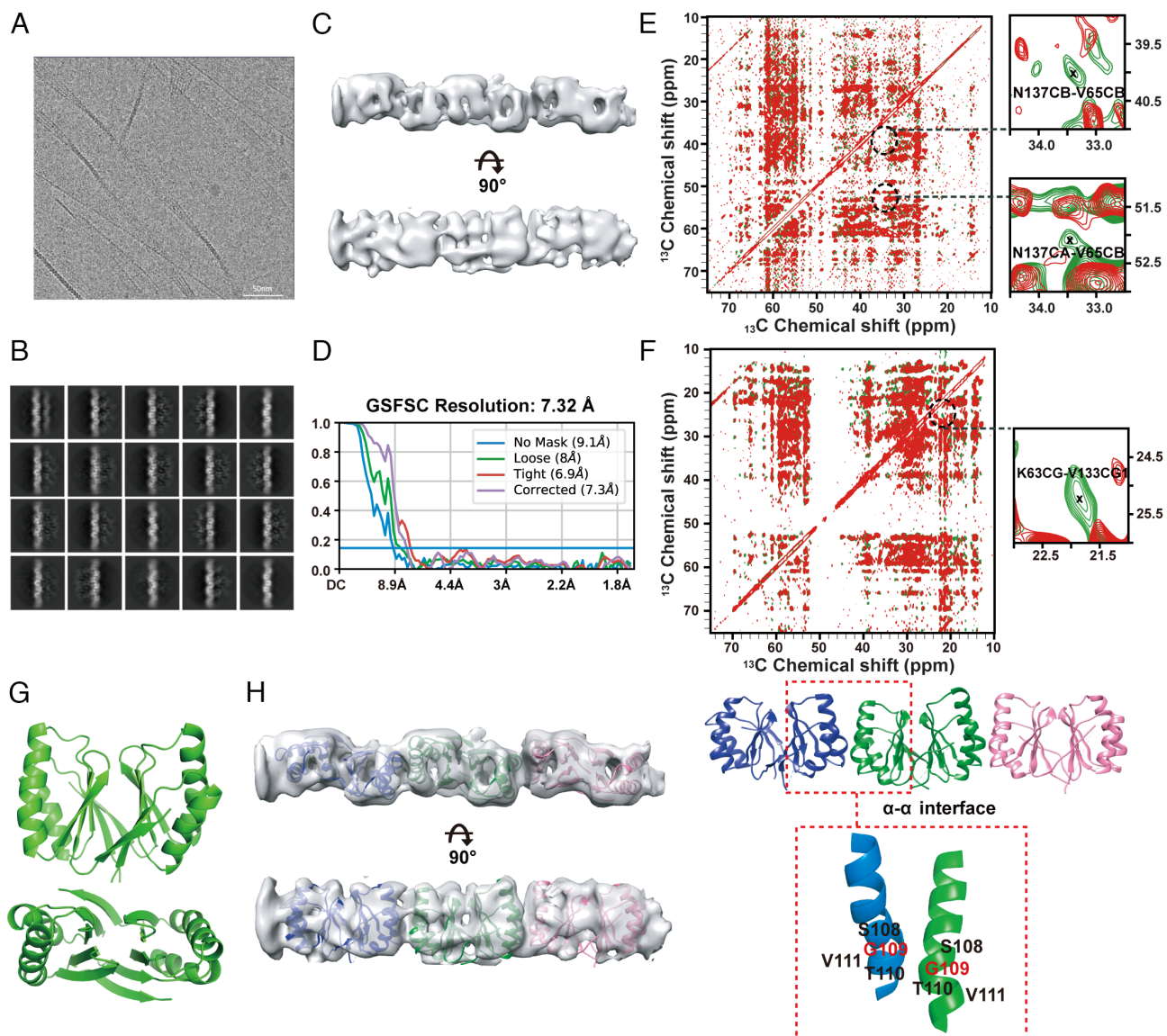


Fig. 3. Structural determination of G137N SepF fibril assembly by a hybrid method combining SSNMR spectroscopy and cryo-EM. (A) Representative cryo-EM micrograph of fibril assembly. (B) Reference-free 2D class averages computed in cryoSPARC. (C) Final 3D reconstruction in two different views. (D) Gold-standard Fourier shell correlation (FSC) plots for the final 3D reconstruction. (E) 2D ^{13}C - ^{13}C CORD spectra of diluted (natural-abundance/ ^{13}C -labeled = 3:1, red) and undiluted (green) sparsely ^{13}C -labeled SepF. Peaks assigned as unambiguous intermolecular distances are enclosed by dashed circles and zoomed in on the Right side. (F) 2D ^{13}C - ^{13}C CORD spectra of diluted (natural-abundance/ ^{13}C -labeled = 3:1, red) and undiluted (green) sparsely 1,3- ^{13}C -labeled SepF. All the unambiguous intermolecular distance constraints shown in the figures were selected according to the following standards: the S/N of peaks in undiluted spectra were larger than 6 and the ΔI (the ratio of S/N of diluted spectra and undiluted spectra after normalization) were below 30%; the symmetrical peaks of them also reached the standards. (G) The best 3D structure model of G137N SepF dimers calculated by CS-Rosetta. (H) Fitting of the SSNMR dimer structure into a cryo-EM map using molecular dynamics flexible fitting (MDFF). The α - α interface is composed of two α -helix 2 from different dimer.

been predicted in our previous study (26). However, a clear inconsistency was found at the fragment of V133-I139, in comparison with the secondary structure predicted by chemical shift-based TALOS+. The segment revealed to be β -strand (β 5) in TALOS+ showed random coil in the CS-ROSETTA structure. We speculated that this phenomenon was most likely caused by the absence of essential contact interfaces with a neighboring monomer. Taking into account that this interface is also essential to form the functional unit of SepF, we set out to calculate the dimeric structure of SepF joined by the β - β interface.

To maintain the basic structural features and enhance the reliability of the structure, several intermolecular distance restraints from the SSNMR spectra and restraints between adjacent residues early in the monomer simulation were incorporated into the procedure. Intermolecular distance restraints were extracted by comparison of ^{13}C - ^{13}C CORD spectra of ^{13}C -glycerol-labeled G137N- SepF diluted or undiluted with natural abundant G137N-SepF (30–32), with a mixing time of 500 ms which was required for long-range distance constraints (SI Appendix, Fig. S13). In SepF assembly, cross peaks in the spectra of undiluted sample can result from intra- as well as intermolecular correlations. In contrast, intermolecular correlations were greatly reduced in the spectra of diluted samples (SI Appendix, Fig. S14). The careful differentiation resulted in three definite intermolecular distance restraints of N137CB-V65CB, N137CA-V65CB, and K63CG-V133CG1 (Fig. 3 E and F and SI Appendix, Table S11). Interestingly, the corresponding residues are all located at β 1 or β 5, fulfilling our demands for information on interface contacts.

After performing calculation, we obtained the 10 best structures that demonstrate the accuracy of the models, with a backbone RMSD of less than 1.5 Å (SI Appendix, Fig. S15). Among these structures, the lowest-energy structure, depicted in Fig. 3G, was selected for flexible fitting. The best G137N SepF dimer structure model obtained by CS-Rosetta was used as the initial structure of MDFF. The MDFF fitting process resulted in a well-refined SepF structure, leading to a final map with an overall cross-correlation coefficient of 0.83, as shown in Fig. 3H. However, there were still a few cryo-EM densities that remained unfilled with the SSNMR structure, attributed to the limited resolution of the cryo-EM data and the inherent flexibility of certain loop regions within the protein. The final map provided detailed information on the α - α interface, which plays a crucial role in the arrangement of SepF dimers. The detection of cross-peaks of intermolecular interactions between the α - α interfaces in the SSNMR spectra posed challenges due to the limited interaction strength and small contact area. Furthermore, distinguishing between intramolecular and intermolecular interactions for the distance constraints involving α 1- α 1 or α 2- α 2 is proved to be a complex task. Despite these challenges, we successfully identified a specific pair of unambiguous intermolecular distance constraints, Y112CA-K83CE, between α 1 and α 2 in the G137N SepF samples (SI Appendix, Fig. S16). This result is in accordance with the structures we have obtained. Additionally, our model exhibited similarities in terms of amino acid composition and folds at the α - α interface (SI Appendix, Fig. S17), in comparison to the crystal structure of *Corynebacterium glutamicum* SepF (16), which is the only structure that available that includes the α - α interface among all species. However, there are slight differences between the angle of the helices, which arise from their difference in species or shape of assembly.

Structure Model of Cyclic Assembly of SepF. As there was no information available on the α - α interface of cyclic SepF, we performed molecular docking to predict the oligomeric structure

of SepF. We applied the SymmDock protocol, a geometry-based rigid-docking method suitable for macromolecules with cyclic symmetries (33, 34), to generate a ring complex by imposing the SepF dimer as an asymmetric subunit. The dimeric WT SepF structure was calculated similarly to G137N SepF, except that the intermolecular distance restraints were derived from ^{13}C - ^{13}C DARR spectra with mixing time of 100, 300, and 500 ms (SI Appendix, Fig. S18). As a result, four definite distance restraints at the β - β interface were obtained for WT SepF: G137CA-L66CB, S136CA-V64CB, S67CA-G137CA, and K63CA-V133CB (Fig. 4A and SI Appendix, Table S13). In addition, we also identified a single pair of intermolecular distance constraints between α 1 and α 2, Y112CA-K83CE (SI Appendix, Fig. S19). The resulting lowest-energy structure was shown in Fig. 4B, and the backbone RMSD between the 10 best structures ranged from 0.5 to 1.1 Å (SI Appendix, Fig. S20). Combing the information from cryo-EM observations, we calculated the number of symmetry dimers according to the practical size of SepF rings. The outer diameter and width of the ring were measured from cryo-EM images (Fig. 4C and SI Appendix, Fig. S21), with an average size of 49.5 nm and 2.4 nm, respectively (Fig. 4D). Meanwhile, the calculated structure yielded a distance of 3.8 nm in the width of the dimer and 2.5 and 2.8 nm in two directions perpendicular to polymer extension directions.

Using the dimeric SepF structure and the number of dimers in the ring as input, SymmDock generated 100 complexes. Of these, credible models were selected based on the correct arrangement, the unambiguous intermolecular distance constraints of Y112CA-K83CE, and well-fitting in diameter and width (SI Appendix, Fig. S22). First, 13 structures were excluded because each dimer was arranged lengthwise, resulting in incorrect width and outer diameters. For most of the other models, the widths of the ring were correct but the outer diameters varied due to the differences in contact interfaces. Two incorrect arrangements with smaller diameters were shown in SI Appendix, Fig. S22 D and E. Specially, two models were also ruled out due to their unreasonable contact interfaces involving α 1- α 1, evidenced by the fact that G109 was determined to be crucial for dimer polymerization. Finally, the remaining nine models were retained for further analysis, and the best complex with the highest score was shown in Fig. 4E. Interestingly, the models showed nearly identical angle formed by adjacent α 2 helices, indicating a small deviation among them (SI Appendix, Fig. S23).

A Putative Mechanism for Curvature Changes of SepF Assembly.

Next, we simulated the assembly of two types of polymers. We compared the structural models of WT- and G137-SepF assembly, with the first α 2 helices fixed, and dimeric SepF copies propagated through the polymerization interfaces (α - α interface) obtained above (Fig. 5). The propagation resulted in an obvious discrepancy in the curvature of two assemblies. For six dimers, a 34° angle was produced by WT- and G137N-SepF assemblies. Importantly, there were no major changes taking place in the overall contour of the assembling unit. Instead, there was a 14° difference in angle between two α helices in the cyclic and fibrillar assemblies. The results from the structural comparison are in good agreement with CSP results in SSNMR, revealing that the shape differences between cyclic and linear assemblies of SepF are caused by the angle changes of α 2. Collectively, we speculate that the substitution of G137 with Gln induces a conformation change of β 1 from the neighboring monomer, followed by a transition to the distant α 1 and α 2. This process is much similar to the “ripple effect,” but the effect is maintained and further induces shape changes of the assembly.

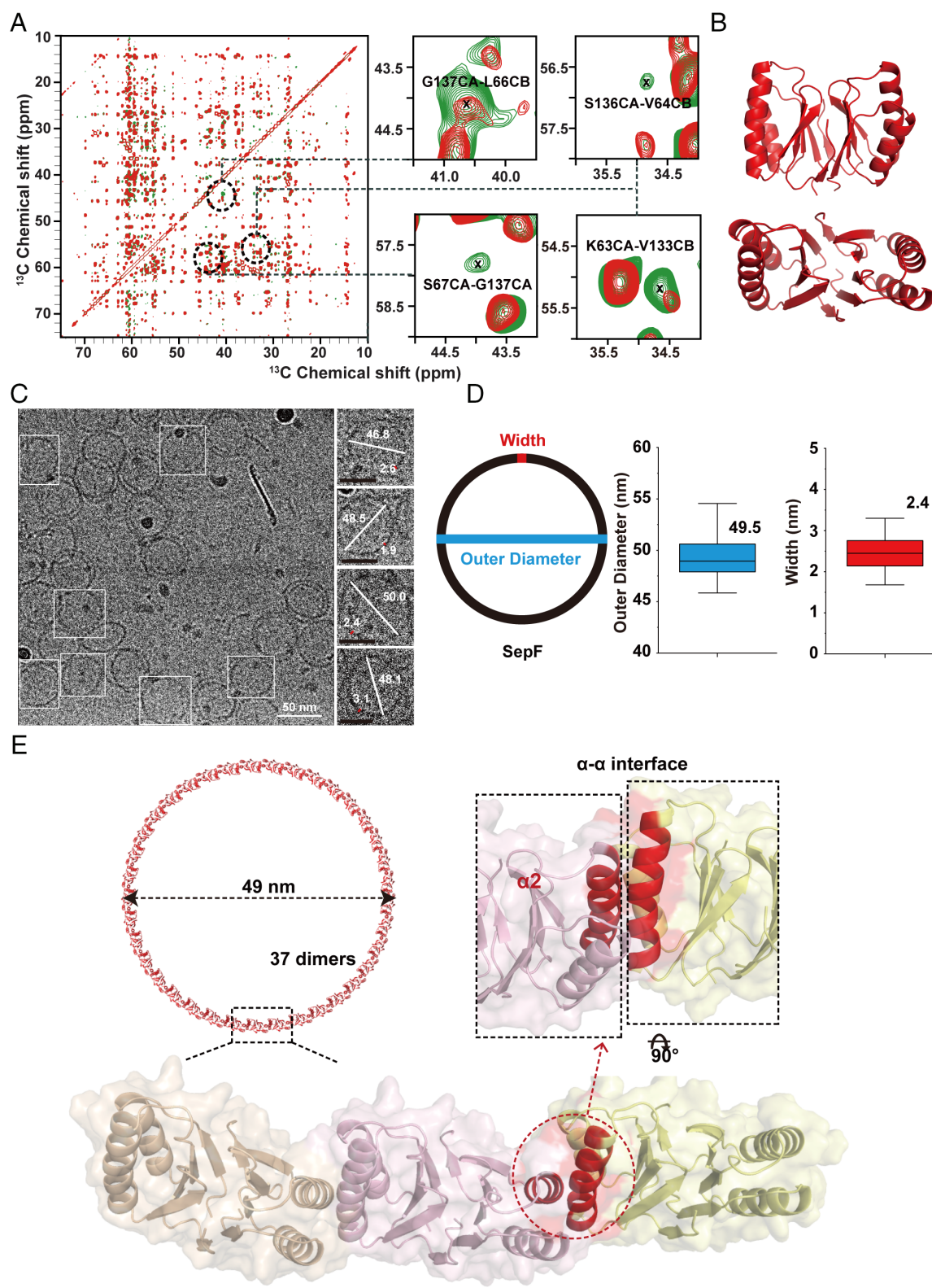


Fig. 4. SymmDock modelization of SepF ring assembly. (A) 2D ^{13}C - ^{13}C DARR spectra of diluted (natural abundance/ ^{13}C -labeled = 3:1, red) and undiluted (green) sparsely $2\text{-}^{13}\text{C}$ -labeled SepF samples. (B) The best 3D structure model of WT SepF dimers calculated by CS-Rosetta. (C) Representative cryo-EM micrograph of ring assembly. The outer diameter and width of single ring were measured using EMAN2. (D) The statistical results of the diameter and width of the ring are shown in box plots. The median of the outer diameter and the width of the ring are 48.94 nm and 2.45 nm, respectively. (E) The highest-scored structure model of the SepF ring was selected for the structural comparison. The ring is composed of 37 dimers, with an outer diameter of 49 nm.

Discussion

SepF polymer formation plays essential roles in gram-positive bacteria, while the curvature of the polymer has been suggested

to control the septal thickness. The structural features of SepF have been previously described, showing that the distinct interfaces in protein polymerization formed by α -helices and β -strands located on different sides of the protein. In this study, we have

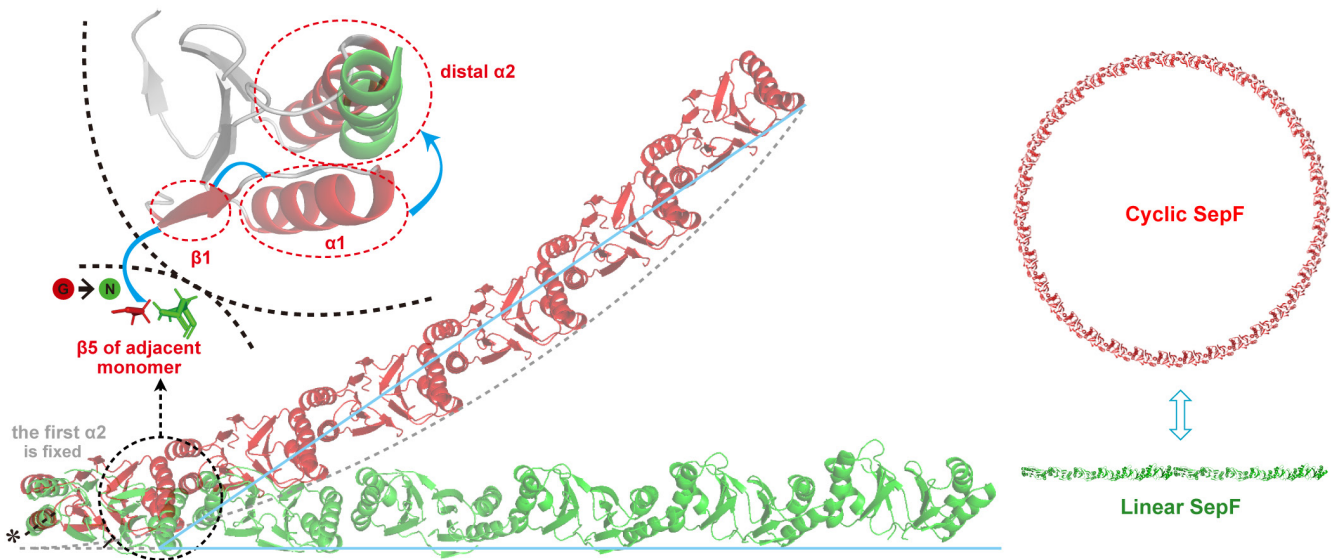


Fig. 5. The mechanism diagram shows the curvature changes from a cyclic ring to a linear fibril of SepF. Mutation on β 5 of the adjacent monomer induces a series of conformation changes, in a way similar to the ripple effect, affecting the orientation of distal α 2 (Top Left). Cumulatively the minor change causes curvature differences between the cyclic and linear assembly, as could be observed when propagated the dimeric SepF copies.

enhanced our understanding of the α - α interface in *B. subtilis* SepF by providing detailed structural information on the contacts involved, highlighting its pivotal role in the curvature of SepF polymerization. Our findings, supported by strong evidence from SSNMR experiments, unveil conformational changes in the α - α interface between cyclic and linear SepF assemblies. Through SSNMR and cryo-EM, we have successfully reconstructed the atomic model of the fibrillar SepF mutant (G137N) and cyclic WT SepF assembly, revealing crucial interactions between two helices of α 2. By comparing the structural models of the linear and cyclic assemblies, we propose that variations in the angular orientation of α 2 directly impact the curvature of the assembly, while the monomer structure of SepF remains largely unaltered. This implies that the α - α interface may be vulnerable to variants and this property may be relevant to the minor changes in ring sizes of SepF from *B. subtilis* and other bacteria species (19).

Initially, the curvature control of SepF was thought to be dominated by the β - β interfaces, and several mutants were made on G137, which was previously shown to be crucial for ring formation of SepF (20). Although the form of the assemblies can be classified, there is no regular patterns according to the properties of amino acid such as polarity and charge. The only pattern we noticed is that the substitutions made by N, K, and R, which lead to linear assembly of SepF, all have an amide group in the terminal of their side chains. Combining the subsequent results of curvature control by α - α contacts, we speculate that mutation on G137 affected the contacts of β 1- β 5 between two monomers. Additional chemical bonds might be formed in the variants of G137N, G137K, and G137R to avoid damage of the β - β interface but at the same time lead to further conformation changes of distant α -helices.

The self-assembly process of protein and peptides can be influenced by many factors including the primary sequence, protein concentration, temperature or other chemicals, but the key issue lies in protein-protein interactions between the assembled units. Based on protein-protein interactions, many kinds of protein structures have been designed in the field of developing biomaterials. At the level of secondary structure motifs, the α -helices formed coiled coil, which account for a significant majority in de novo design compared to β -sheets, due to structural and geometric considerations (35, 36). From this perspective, our findings verified

that α -helices offer more possibilities for geometric and topological arrangements than β -sheet structures. However, self-assembly in nature is complicated and functionally relevant under precise regulation. In bacteria flagellum and the type III secretion system, both α -helices and β -strands take part in ring formation (37–39), but the mechanism of curvature formation has not been clearly stated. On the other hand, the structural flexibility of the monomer structure in ESCRT-III and PspA/Vipp1 has been proven to affect the curvature of polymer structures (10–12). Our investigations here represented a clear picture of curvature changes by slight angular changes of α -helix, although the linear assembly of SepF is not relevant to the physiological process.

We used a combination of SSNMR, cryo-EM, and molecular modeling to compare the structural details of cyclic and linear assembly. Integrating these approaches overcome their individual limitations and enables atomic-resolution structure determination of protein assemblies (28, 29, 40–42). The low resolution of the cryo-EM map in this work reflects the large number of deposited maps in the EM database. For SSNMR, the biggest obstacle comes from the difficulty in obtaining sufficient useful restraints due to sensitivity and signal overlap on larger proteins. However, MAS SSNMR for biological samples offers the possibility to refine the average structural picture, attributed to the sensitivity of NMR parameters to local structural environments. Among these parameters, chemical shifts are the most readily and accurately measured, with specificity affected by conformation changes in proteins (43, 44). Although we used molecular modeling in integrating SSNMR and EM experimental data, the key structural features of the cyclic and linear SepF assemblies were determined by experimental observations. Specifically, the structural units of these assemblies were from CS-Rosetta calculations, which are based on experimentally observed chemical shifts and distance restraints, without the assistance of the available X-ray structures. The assembled patterns of these units in assemblies were determined by EM observations, such as EM electron density map of the linear assembly and diameter, width of the cyclic assembly.

Collectively, we investigated the role of a key residue, Gly137, located on the β - β contacts defining the structural unit of SepF, in remodeling the shape of the protein assembly. By comparing the chemical shifts of cyclic or linear SepF assemblies, we demonstrated

that the conformational change of the α - α interface between the structural units was a decisive factor for shape changes. The CS-Rosetta models of G137N SepF, calculated based on the chemical shifts and unambiguous distance constraints from SSNMR experiments, combined well with the cryo-EM density and showed atomic details of the α - α interface of the linear assembly. Together with the SymmDock results of cyclic WT SepF, we proposed a mechanism model for the curvature changes of SepF assemblies. The high quality of SSNMR spectra ensured the high reliability of CSPs results and structural models, and the two sets of results corroborate each other. The present study highlights the effect of α -helical contacts on the curvature of the assemblies, providing a perspective on biological regulation and insights into the design aspects of protein self-assemblies.

Materials and Methods

Sample Preparation. The expression and purification of *B. subtilis* SepF (57–151) were performed as published previously (26). Briefly, all mutants for SepF-G137 were generated by PCR-based site-directed mutagenesis. WT SepF and the variants proteins were expressed in *E. coli* C43 (DE3) or BL21 (DE3) cells. For isotope labeling samples, the proteins were expressed in freshly prepared M9 medium containing 4 g/L ^{15}N -ammonium chloride and 2 g/L ^{13}C -glucose (or [2- ^{13}C]-glycerol and [1,3- $^{13}\text{C}_2$]-glycerol for sparse labeling). After expression, cells were harvested and sonicated in lysis buffer (25 mM Tris-HCl, 1 mM EDTA, pH 8.5). The supernatant was obtained and subjected to ammonium sulfate precipitation using a final concentration of ~25% w/v. The precipitate was collected and dissolved in a urea solution (8 mM urea, 25 mM Tris, and 1 mM EDTA, pH 8.5). The filtered supernatant was concentrated and loaded onto a HiLoadTM 16/60 SuperdexTM 200 PG column (GE Healthcare). The fraction containing SepF protein was collected and assessed by SDS-PAGE.

Polymerization of SepF was achieved by dialysis against lysis buffer for 2 d at 18 °C. The characterization of all constructs, including Gel Filtration Assays, Circular Dichroism, and Transmission Electron Microscopy, is given in *SI Appendix*.

SSNMR. For SSNMR experiments, the protein assemblies were pelleted by centrifugation at 548,352 $\times g$ for 3 h and packed into the 3.2-mm rotor. 2D ^{13}C - ^{13}C DARR and CORD spectra for distance constraint assignments and G137R SepF 3D spectra were measured at 273 K on an 800 MHz (18.8 T) Bruker Avance III spectrometer using a 3.2-mm E-free ^1H / ^{13}C / ^{15}N probe at a MAS frequency of 10,500 Hz. Other SSNMR spectra for chemical shift assignments were measured at 273 K on a 600-MHz (14.1 T) Varian VNMRS spectrometer using a 3.2-mm ^1H / ^{13}C / ^{15}N triple-resonance BIO-MAS probe at an 11,111 Hz MAS speed. The typical 90° widths of ^1H / ^{13}C / ^{15}N nuclei were 3.2 μs , 7.2 μs , and 7.5 μs for the Varian 600 MHz spectrometer and 3.1 μs , 4.2 μs , and 6.7 μs for the Bruker 800 MHz spectrometer, respectively. The ^{13}C chemical shifts were referenced using the methylene resonance of adamantine (40.48 ppm), and the ^{15}N chemical shifts were referenced using the liquid NH₃ resonance according to the gyromagnetic ratio of ^{13}C / ^{15}N . Detailed parameters and analysis of SSNMR spectra can be found in *SI Appendix*.

1. P. Ge, Z. H. Zhou, Hydrogen-bonding networks and RNA bases revealed by cryo electron microscopy suggest a triggering mechanism for calcium switches. *Proc. Natl. Acad. Sci. U.S.A.* **108**, 9637–9642 (2011).
2. S. O. Andersen, P. Hojrup, P. Roepstorff, Insect cuticular proteins. *Insect Biochem. Mol. Biol.* **25**, 153–176 (1995).
3. J. A. Fallas *et al.*, Computational design of self-assembling cyclic protein homo-oligomers. *Nat. Chem.* **9**, 353–360 (2017).
4. D. S. Goodsell, J. A. Olson, Structural symmetry and protein function. *Annu. Rev. Biophys. Biomol. Struct.* **29**, 105–153 (2000).
5. M. Simunovic *et al.*, How curvature-generating proteins build scaffolds on membrane nanotubes. *Proc. Natl. Acad. Sci. U.S.A.* **113**, 11226–11231 (2016).
6. W. A. Prinz, J. E. Hinshaw, Membrane-bending proteins. *Crit. Rev. Biochem. Mol. Biol.* **44**, 278–291 (2009).
7. B. J. Pieters, M. B. van Eldijk, R. J. Nolte, J. Mecinovic, Natural supramolecular protein assemblies. *Chem. Soc. Rev.* **45**, 24–39 (2016).
8. M. M. Hingorani, M. O'Donnell, A tale of toroids in DNA metabolism. *Nat. Rev. Mol. Cell Biol.* **1**, 22–30 (2000).
9. A. K. Pfitzner, J. Moser von Filseck, A. Roux, Principles of membrane remodeling by dynamic ESCRT-III polymers. *Trends Cell Biol.* **31**, 856–868 (2021).
10. T. K. Gupta *et al.*, Structural basis for Vipp1 oligomerization and maintenance of thylakoid membrane integrity. *Cell* **184**, 3643–3659.e3623 (2021).

Cryo-EM Grid Preparation and Data Acquisition. Purified sample was used for cryo-EM grid preparation and data collection. Briefly, Quantifoil 300 mesh Cu/2 holey carbon grid (Quantifoil Micro Tools GmbH) was glow-discharged using PELOCO easiGlow (Ted Pella) for 1 min under the current of 15 mA. Four μL aliquot of the purified sample was applied onto the processed grid and plunge frozen in liquid ethane precooled by liquid nitrogen under 4 °C and 100% humidity controlled by Vitrobot Mark IV (Thermo Fisher Scientific). The prepared cryo-EM grids were further loaded onto a Titan krios G3i transmission electron microscope (Thermo Fisher Scientific) for sample screening. Grids with suitable ice thickness and sample concentration were used for data collection. A total of 4,845 movie stacks were collected using Titan krios G3i operated under 300 kV, equipped with the Gatan K2 summit detector (Gatan). Inelastic scattered electrons were filtered using the Gatan GIF Quantum energy filter (Gatan) with 20 eV slit width. Data collection was controlled by SerialEM. The nominal magnification was 165,000 \times , corresponding to a calibrated pixel size of 0.829 Å. The nominal defocus value range was from −1.5 to −2.5 μm . Each movie stack contains 32 frames, and each frame was exposed for 0.106 s with a dose rate of 14.7 e/Å², resulting in the total dose of 50 e/Å² for each movie stack.

Data, Materials, and Software Availability. The SSNMR data have been deposited to the Biological Magnetic Resonance Bank under accession codes 36538 (45) for WT, 36539 (46) for G137N, and 51778 (47) for G137F SepF. The SSNMR structures are available from the Protein Data Bank (www.rcsb.org), under accession numbers 8HQZ (48) for the WT and 8HZT (49) for G137N SepF. The cryo-EM structure of G137N SepF has been deposited to the Electron Microscopy Data Bank under accession code EMD-35112 (50). All other data are included in the manuscript and/or *SI Appendix*.

ACKNOWLEDGMENTS. We are grateful for the National Natural Science Foundation of China (21927801, 21991801, 21921004, 31900046, 81972085, and 82172465), the Chinese Academy of Sciences (YJKYYQ20190032), and Guangdong Provincial Key Laboratory of Advanced Biomaterials (2022B1212010003). We thank Yi Guo from the Center for Materials Research and Analysis in the Wuhan University of Technology for the help on transmission electron microscopy. We are very grateful to Dr. Yang Shen (NIH) for assistance in CS-Rosetta calculations.

Author affiliations: ^aNational Center for Magnetic Resonance in Wuhan, Key Laboratory of Magnetic Resonance in Biological Systems, State Key Laboratory of Magnetic Resonance and Atomic and Molecular Physics, Wuhan Institute of Physics and Mathematics, Innovation Academy for Precision Measurement Science and Technology, Chinese Academy of Sciences, Wuhan 430071, People's Republic of China; ^bUniversity of Chinese Academy of Sciences, Beijing 100049, People's Republic of China; ^cShenzhen Institute of Advanced Technology, Chinese Academy of Sciences, Shenzhen 518055, People's Republic of China; ^dSouthern University of Science and Technology, Shenzhen 518055, People's Republic of China; ^eDepartment of Orthopedics, Shenzhen Intelligent Orthopaedics and Biomedical Innovation Platform, Guangdong Provincial Research Center for Artificial Intelligence and Digital Orthopedic Technology, Shenzhen Second People's Hospital, The First Affiliated Hospital of Shenzhen University, Shenzhen 518000, People's Republic of China; and ^fInterdisciplinary Institute of NMR and Molecular Sciences, School of Chemistry and Chemical Engineering, The State Key Laboratory of Refractories and Metallurgy, Wuhan University of Science and Technology, Wuhan 430081, People's Republic of China

11. B. Junglas *et al.*, PspA adopts an ESCRT-III-like fold and remodels bacterial membranes. *Cell* **184**, 3674–3688.e3618 (2021).
12. J. Liu *et al.*, Bacterial Vipp1 and PspA are members of the ancient ESCRT-III membrane-remodeling superfamily. *Cell* **184**, 3660–3673.e3618 (2021).
13. Y. Bai, Q. Luo, J. Liu, Protein self-assembly via supramolecular strategies. *Chem. Soc. Rev.* **45**, 2756–2767 (2016).
14. J. D. Hartgerink, E. Beniash, S. I. Stupp, Self-assembly and mineralization of peptide-amphiphile nanofibers. *Science* **294**, 1684–1688 (2001).
15. O. Keskin, A. Gursoy, B. Ma, R. Nussinov, Principles of protein–protein interactions: What are the preferred ways for proteins to interact? *Chem. Rev.* **108**, 1225–1244 (2008).
16. A. Sogues *et al.*, Essential dynamic interdependence of FtsZ and SepF for Z-ring and septum formation in *Corynebacterium glutamicum*. *Nat. Commun.* **11**, 1641 (2020).
17. R. Duman *et al.*, Structural and genetic analyses reveal the protein SepF as a new membrane anchor for the Z ring. *Proc. Natl. Acad. Sci. U.S.A.* **110**, E4601–E4610 (2013).
18. N. Pende *et al.*, SepF is the FtsZ anchor in archaea, with features of an ancestral cell division system. *Nat. Commun.* **12**, 3214 (2021).
19. M. Wenzel *et al.*, Control of septum thickness by the curvature of SepF polymers. *Proc. Natl. Acad. Sci. U.S.A.* **118**, e202635118 (2021).
20. M. E. Gundogdu *et al.*, Large ring polymers align FtsZ polymers for normal septum formation. *EMBO J.* **30**, 617–626 (2011).

21. Y. Shen *et al.*, Consistent blind protein structure generation from NMR chemical shift data. *Proc. Natl. Acad. Sci. U.S.A.* **105**, 4685–4690 (2008).
22. Y. Zhao *et al.*, Gating mechanism of Aquaporin Z in synthetic bilayers and native membranes revealed by solid-state NMR spectroscopy. *J. Am. Chem. Soc.* **140**, 7885–7895 (2018).
23. A. R. Cormier, X. Pang, M. L. Zimmerman, H. X. Zhou, A. K. Paravastu, Molecular structure of RADA16-I designer self-assembling peptide nanofibers. *ACS Nano* **7**, 7562–7572 (2013).
24. K. Nagy-Smith, E. Moore, J. Schneider, R. Tycko, Molecular structure of monomeric peptide fibrils within a kinetically trapped hydrogel network. *Proc. Natl. Acad. Sci. U.S.A.* **112**, 9816–9821 (2015).
25. A. Micsonai *et al.*, Accurate secondary structure prediction and fold recognition for circular dichroism spectroscopy. *Proc. Natl. Acad. Sci. U.S.A.* **112**, E3095–E3103 (2015).
26. C. Zhang *et al.*, Structural insights into the interaction between *Bacillus subtilis* SepF assembly and FtsZ by solid-state NMR spectroscopy. *J. Phys. Chem. B* **126**, 5219–5230 (2022).
27. R. Gao *et al.*, A prototype protein nanocage minimized from carboxysomes with gated oxygen permeability. *Proc. Natl. Acad. Sci. U.S.A.* **119**, e2104964119 (2022).
28. L. Sborgi *et al.*, Structure and assembly of the mouse ASC inflammasome by combined NMR spectroscopy and cryo-electron microscopy. *Proc. Natl. Acad. Sci. U.S.A.* **112**, 13237–13242 (2015).
29. J. P. Demers *et al.*, High-resolution structure of the Shigella type-III secretion needle by solid-state NMR and cryo-electron microscopy. *Nat. Commun.* **5**, 4976 (2014).
30. P. Lundstrom *et al.*, Fractional ^{13}C enrichment of isolated carbons using $[^{1-13}\text{C}]$ - or $[^{2-13}\text{C}]$ -glucose facilitates the accurate measurement of dynamics at backbone $\text{C}\alpha\text{H}$ and side-chain methyl positions in proteins. *J. Biomol. NMR* **38**, 199–212 (2007).
31. A. Loquet, K. Giller, S. Becker, A. Lange, Supramolecular interactions probed by ^{13}C – ^{13}C solid-state NMR spectroscopy. *J. Am. Chem. Soc.* **132**, 15164–15166 (2010).
32. A. Loquet, G. Lv, K. Giller, S. Becker, A. Lange, ^{13}C spin dilution for simplified and complete solid-state NMR resonance assignment of insoluble biological assemblies. *J. Am. Chem. Soc.* **133**, 4722–4725 (2011).
33. D. Schneidman-Duhovny, Y. Inbar, R. Nussinov, H. J. Wolfson, Geometry-based flexible and symmetric protein docking. *Proteins* **60**, 224–231 (2005).
34. D. Schneidman-Duhovny, Y. Inbar, R. Nussinov, H. J. Wolfson, PatchDock and SymmDock: Servers for rigid and symmetric docking. *Nucleic Acids Res.* **33**, W363–W367 (2005).
35. W. Zhou, T. Smidlehner, R. Jerala, Synthetic biology principles for the design of protein with novel structures and functions. *FEBS Lett.* **594**, 2199–2212 (2020).
36. D. W. Adams, J. Errington, Bacterial cell division: Assembly, maintenance and disassembly of the Z ring. *Nat. Rev. Microbiol.* **7**, 642–653 (2009).
37. J. Tan *et al.*, Structural basis of assembly and torque transmission of the bacterial flagellar motor. *Cell* **184**, 2665–2679.e2619 (2021).
38. J. R. C. Bergeron, T. C. Marlovits, Cryo-EM of the injectisome and type III secretion systems. *Curr. Opin. Struct. Biol.* **75**, 102403 (2022).
39. M. Lunelli *et al.*, Cryo-EM structure of the *Shigella* type III needle complex. *PLoS Pathog.* **16**, e1008263 (2020).
40. D. F. Gaulto *et al.*, Integrated NMR and cryo-EM atomic-resolution structure determination of a half-megadalton enzyme complex. *Nat. Commun.* **10**, 2697 (2019).
41. X. Wu *et al.*, The structure of a minimum amyloid fibril core formed by necrosis-mediating RHIM of human RIPK3. *Proc. Natl. Acad. Sci. U.S.A.* **118**, e2022933118 (2021).
42. T. Thamees *et al.*, Curvature of the retroviral capsid assembly is modulated by a molecular switch. *J. Phys. Chem. Lett.* **12**, 7768–7776 (2021).
43. A. Cavalli, X. Salvatella, C. M. Dobson, M. Vendruscolo, Protein structure determination from NMR chemical shifts. *Proc. Natl. Acad. Sci. U.S.A.* **104**, 9615–9620 (2007).
44. P. Robustelli, K. A. Stafford, A. G. Palmer IIIrd, Interpreting protein structural dynamics from NMR chemical shifts. *J. Am. Chem. Soc.* **134**, 6365–6374 (2012).
45. W. Liu, J. Yang, *Bacillus subtilis* SepF protein assembly (wild type). Biological Magnetic Resonance Bank. https://bmrbl.io/data_library/summary/index.php?bmrblid=36538. Deposited 9 January 2023.
46. W. Liu, J. Yang, *Bacillus subtilis* SepF protein assembly (G137N mutant). Biological Magnetic Resonance Bank. https://bmrbl.io/data_library/summary/index.php?bmrblid=36539. Deposited 9 January 2023.
47. W. Liu, C. Zhang, J. Yang, SepF protein assembly G137F mutant. Biological Magnetic Resonance Bank. https://bmrbl.io/data_library/summary/index.php?bmrblid=51778. Deposited 14 January 2023.
48. W. Liu, J. Yang, *Bacillus subtilis* SepF protein assembly (G137N mutant). RCSB Protein Data Bank. <https://www.rcsb.org/structure/8HZQ>. Deposited 9 January 2023.
49. W. Liu, J. Yang, *Bacillus subtilis* SepF protein assembly (wild type). RCSB Protein Data Bank. <https://www.rcsb.org/structure/8HZT>. Deposited 9 January 2023.
50. H. Zhang, C. Zhang, Z. Chang, J. Yang, Cryo-EM map of SepF. Electron Microscopy Data Bank. <https://www.ebi.ac.uk/emdb/EMD-35112>. Deposited 1 November 2023.